Fourier-domain image reconstruction in near-field microwave imaging using a dynamic metasurface antenna: a sparse-sampling-based approach

Amir Masoud Molaei*[a], Vasiliki Skouroliakou[a], Vincent Fusco[a], Okan Yurduseven[a]
[a]Institute of Electronics, Communications and Information Technology (ECIT), Queen's University Belfast, Queen's Road, Belfast, U.K. BT3 9DT

ABSTRACT

In recent years, dynamic metasurface antennas (DMAs) have been proposed as an efficient alternative platform for computational imaging, which can drastically simplify the hardware architecture. In this paper, we first mathematically describe the existing solution to be able to convert raw measurements obtained by a DMA in the frequency-space domain into raw data on Fourier bases. Next, an optimization problem based on compressive sensing theory is defined, through which only a limited share of the total frequency/spatial data will be needed. The converted/retrieved data are used to reconstruct the image in the Fourier domain. The performance of the corresponding image reconstruction techniques (with/without Stolt interpolation operation) is evaluated in terms of the quality of the reconstructed image (both visually and quantitatively) and computational time with computer simulations.

Keywords: Compressive sensing, DMA, Fourier-domain image reconstruction, near-field microwave imaging

1. INTRODUCTION

The application of microwave imaging in various fields has led to significant improvements in radar imaging both in the physical and processing layers [1-5]. Although the electronic scanning mechanism can be a suitable choice to improve the data acquisition time in microwave imaging, conventional array antennas are expensive and heavy, and usually have high power consumption (due to the need for complex control circuitry and power-hungry radio frequency components) [6].

Recently, dynamic metasurface antennas (DMAs) have been proposed as an efficient alternative platform for computational imaging, which can greatly simplify the hardware architecture [7, 8]. However, since they do not produce uniform radiation patterns due to a physical layer compression, the raw data provided by them are not directly suitable for use in computationally efficient fast Fourier-based scene image reconstruction techniques [9-11].

In this paper, we will show how raw measurements obtained by DMA in the frequency-space domain can be converted to raw data on Fourier bases. In such a structure, reconstructing a three-dimensional (3-D) image of the scene requires performing full scanning in numerous uniform spatial-frequency steps [12]. In the presented approach, by defining an optimization problem based on compressed sensing (CS), only a limited share of the total frequency and/or spatial data will suffice. This allows us to skip full scanning without worrying about violating the Nyquist criterion, thus significantly increasing the data acquisition rate. The converted-retrieved data are employed to reconstruct the image in the Fourier domain by means of two algorithms (one using Stolt interpolation operation and the other using range stacking). The performance of the corresponding image reconstruction algorithms is evaluated in terms of the quality of the reconstructed image and computational time with computer simulations.

The rest of this paper is organized as follows: in Section 2, the system and data model are presented; Section 3 details the image reconstruction algorithms; Section 4 is devoted to the presentation of simulation results and analyzes; Section 5 provides a brief conclusion.

*a.molaei@qub.ac.uk; fax 44 28 9097 1702; pure.qub.ac.uk/en/persons/amir-masoud-molaei

2. SYSTEM AND DATA MODEL

Figure 1 shows the general structure of the imaging system considered in this paper. The system uses a fixed DMA along the x-axis (horizontal) as the transmitter (Tx), and a single antenna moving along the y-axis (vertical) as the receiver (Rx). The DMA consists of a 1D microstrip waveguide with N_T complementary electric-LC (cELC) metamaterial resonators placed at a subwavelength distance of d_T from each other [3, 13]. Each cELC resonator (element) can be randomly turned on/off by an external stimulus. This can lead to the generation of a set of masks that correspond to diverse and distinct spatial radiation patterns [14]. It should be noted here that although the cELC topology is considered as the resonator element forming the DMA architecture in this work, the presented approach can be adopted to other types of DMAs synthesized using different resonator elements without loss of generality. At a given frequency f multiple measurements can be made by cycling through M masks (tuning modes). To comply with the Nyquist rate and benefit from fast Fourier calculations, it is necessary to perform spatial sampling (i.e. vertical scanning) and frequency sampling uniformly and with limited intervals. However, in this case, the full data acquisition process can be too time-consuming. As a solution, we assume here that spatial/frequency sampling is performed non-uniformly (randomly) with a much smaller number of samples (at a given CS rate) compared to full sampling. Figure 1 shows the mechanical scan points in blue, and the sampling points skipped in red.

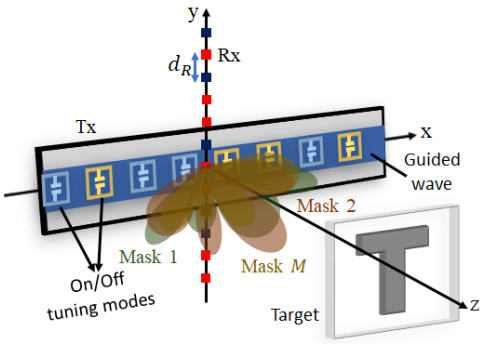

Figure 1. The general structure of the imaging system.

The measurement signal with the presence of DMA has a more complicated form than the total field that is conventionally calculated for the model of single dipoles only with Green's function G [15]. Assuming full sampling, the measurement signal g in the scenario of this paper can be written in the following form [3]:

$$g(f)=\int_x\int_y\int_z U_T(\vec{r},f)\rho(\vec{r})G(\vec{r},y_{i'},f)\,dz\,dy\,dx, \tag{1}$$

where $\vec{r}$ is the position vector to a point in the scene, ρ denotes the reflectivity of the target, and $y_{i'}$ represents the position of the i'-th sampling point of the Rx, where $i'=1,2,...,N_R$ and N_R is the total number of spatial sampling points in the vertical direction. Under the first Born approximation, U_T is the field radiated from the aperture, which can be expressed as a superposition of all metamaterial elements (see [16, 17] for details).

3. IMAGE RECONSTRUCTION ALGORITHMS

Assuming that the signal measured in the aperture plane can be expanded in terms of the fields corresponding to all masks ($m=1,...,M$), we can write [3, 18]

$$g_{m,i'}(f)=\sum_{i=1}^{N_T}\Phi_m(x_i,f)\,s(x_i,y_{i'},f),\quad i=1,...,N_T, \tag{2}$$

where Φ_m and s represents the field over the aperture for the m-th mask and total field (incident field), respectively. By creating a set of aperture modes with some degrees of orthogonality, using the screening property of the delta function, and applying some mathematical simplifications, (2) can be written in matrix form as [3, 19]

$$\mathbf{s}(f) = \mathbf{\Phi}^{\dagger}(f)\mathbf{g}(f), \tag{3}$$

where $\mathbf{s}(f) \in \mathbb{C}^{N_T \times N_R}$, $\mathbf{\Phi}(f) \in \mathbb{C}^{M \times N_T}$ and $\mathbf{g}(f) \in \mathbb{C}^{M \times N_R}$. Note that in the case of recovering aperture fields, they can be predicted if there is a suitable forward model of the aperture [20]. In practice, a set of near-field (NF) scans is usually performed along the length of the aperture for each of the tuning modes, providing a set of complex field values [20]. For more details about the aperture field matrix, refer to [19, 20].

The data are now in the form required for use by fast Fourier-based techniques. According to the geometry of the system, the signal s can be written as follows:

$$s(x_i, y_{i'}, f) = \iiint_{x\ y\ z} \frac{\rho(x,y,z)}{16\pi^2 R_i R_{i'}} e^{-jkR_i} e^{-jkR_{i'}} \delta(y_i, z_i)\, \delta(x_{i'}, z_{i'})\, dz\, dy\, dx, \tag{4}$$

where R_i and $R_{i'}$ represent the distances between Tx positions (i.e. (x_i, y_i, z_i)) and Rx positions (i.e. $(x_{i'}, y_{i'}, z_{i'})$) to the target points, respectively. By taking the 2-D Fourier transform (FT) from both sides of (4) on the aperture coordinates, employing the convolution theorem and the method of stationary phase [18], and applying some mathematical approximations and simplifications, the representation of the signal s in the wavenumber domain can be written as follows (see [12, 19] for more details):

$$S(k_x, k_y, k) = \frac{-j}{32\pi k \left(k^2 - k_x^2\right)^{\frac{1}{4}} \left(k^2 - k_y^2\right)^{\frac{1}{4}}} \iiint_{x\ y\ z} \rho(x,y,z)\, e^{-jk_x x} e^{-jk_y y} e^{-j\left(\sqrt{k^2-k_x^2}+\sqrt{k^2-k_y^2}\right)z}\, dz\, dy\, dx, \quad k^2 \geq k_x^2, k^2 \geq k_y^2. \tag{5}$$

In the above equation, the term $-j\pi \Big/ \left(2k\left(k^2 - k_x^2\right)^{1/4}\left(k^2 - k_y^2\right)^{1/4}\right)$ acts as a filter in the Fourier domain. Suppose we denote the output signal obtained by applying filtering to $S(k_x, k_y, k)$ with $\overline{S}(k_x, k_y, k)$. This filtering is performed using the appropriate amplitude term mentioned above, as well as backpropagating the signal to the center of the defined scene in the range z_0 (also called motion compensation [21]). In this way, (5) can be rewritten as follows:

$$\overline{S}(k_x, k_y, k) = \frac{1}{16\pi^2} \iiint_{x\ y\ z} \rho(x,y,z)\, e^{-jk_x x} e^{-jk_y y} e^{-j\left(\sqrt{k^2-k_x^2}+\sqrt{k^2-k_y^2}\right)z}\, dz\, dy\, dx, \quad k^2 \geq k_x^2, k^2 \geq k_y^2. \tag{6}$$

Reflectivity information can be extracted from (6) in several ways. From (6), it can be concluded that to recover the target reflectivity by taking advantage of fast Fourier calculations, a 3-D inverse FT (IFT) should be applied to the signal $\tilde{S}(k_x, k_y, k_z)$, where $\tilde{S}(k_x, k_y, k_z)$ is the signal mapped from $\overline{S}(k_x, k_y, k)$ upon defining dispersion relation $k_z \triangleq \sqrt{k^2 - k_x^2} + \sqrt{k^2 - k_y^2}$ with an equispaced distribution vector [22]. Such mapping is known as Stolt interpolation [23] in the literature. In closed form

$$\rho(x,y,z) \simeq \text{IFFT}_{k_x, k_y, k_z}\left\{\tilde{S}(k_x, k_y, k_z)\right\}. \tag{7}$$

The second way, which does not require the Stolt interpolation operation, is to stack the information of signal $\overline{S}(k_x, k_y, k)$ on a defined range grid of length N_z and then apply 2-D IFT to the corresponding cross-range information; that's mean:

$$\rho(x,y,z) \simeq \text{IFFT}_{k_x, k_y}\left\{\sum_{l=1}^{N_z} \overline{S}(k_x, k_y, k) e^{jk_z z_l}\right\}. \tag{8}$$

Apart from the above, the use of non-uniform IFT [3, 24] can also be considered as another way to extract reflectivity information.

As mentioned in the previous section, full sampling/scanning in the introduced system may not provide the desired information acquisition rate. This issue can be alleviated by defining a minimization problem using CS theory so that

there is no need to collect numerous data at the Nyquist rate. Suppose that $\mathbf{s}$ exhibits sparsity on a certain orthonormal basis $\boldsymbol{\psi}$ [25]. By arranging $\mathbf{s}$ as a column vector (i.e. $\widehat{\mathbf{s}} \in \mathbb{C}^{N_T N_R N_f \times 1}$, where N_f denotes the total number of frequency samples), it can be represented as a compressible signal using its sparse transform domain vector $\boldsymbol{\theta}$ [26]

$$\widehat{\mathbf{s}} = \boldsymbol{\psi}_{N_T N_R N_f \times N_T N_R N_f} \boldsymbol{\theta}_{N_T N_R N_f \times 1}. \tag{9}$$

Let us denote a set of randomly chosen reduced measurements by

$$\mathbf{s}'(f) \triangleq \boldsymbol{\Phi}'^{\dagger}(f)\mathbf{g}'(f), \tag{10}$$

where $\mathbf{s}'(f) \in \mathbb{C}^{N_T \times M_R}$, $\boldsymbol{\Phi}'(f) \in \mathbb{C}^{M \times N_T}$, $\mathbf{g}'(f) \in \mathbb{C}^{M \times M_R}$, $M_R < N_R$ and $M_f < N_f$. According to (9), the column vector of $\mathbf{s}' \in \mathbb{C}^{N_T \times M_R \times M_f}$ (i.e. $\widetilde{\mathbf{s}}' \in \mathbb{C}^{N_T M_R M_f \times 1}$) can be modeled by projecting $\widehat{\mathbf{s}}$ onto the vectors $\left\{\boldsymbol{\gamma}_1, ..., \boldsymbol{\gamma}_{N_T M_R M_f}\right\}$ that form the measurement matrix $\boldsymbol{\Gamma}$

$$\widetilde{\mathbf{s}}' = \boldsymbol{\Gamma}_{N_T M_R M_f \times N_T N_R N_f} \widehat{\mathbf{s}} = \mathbf{A}_{N_T M_R M_f \times N_T N_R N_f} \boldsymbol{\theta}, \tag{11}$$

where $\mathbf{A} = \boldsymbol{\Gamma}\boldsymbol{\psi}$ is the sensing matrix [27]. The recovery problem can be described as the following convex ℓ_1-minimization [28]:

$$\min \left\|\boldsymbol{\theta}\right\|_1 \text{ s.t. } \widetilde{\mathbf{s}}' = \mathbf{A}\boldsymbol{\theta}. \tag{12}$$

4. SIMULATION RESULTS AND DISCUSSION

In this section, the results of numerical simulations are given along with related discussions. All computations are performed in MATLAB R2022b running on a 64-bit Windows 11 operating system with 16 GB of random access memory and a Core-i7 central processing unit at 2.8 GHz. $\boldsymbol{\Gamma}$ is designed in such a way that only one 1 is placed at random with a uniform distribution in each row and the rest of the entries are 0. Based on previous studies [3, 29], for the dictionary matrix, the discrete Fourier transform (DFT) domain is considered. To perform CS reconstruction in (12), convex programming [30], or as an alternative, greedy algorithms [31] can be used. In general, greedy algorithms are computationally fast, however, their reconstruction errors are relatively larger than ℓ_1-norm solutions [32]. Convex relaxations have better theoretical guarantees and recoverability but are more time-consuming [32]. Due to computational considerations, we use the smoothed ℓ_0 (SL0) algorithm [33] for data retrieval in this paper.

The simulation parameters are given in Table I, where λ, Q, Z_0, n_g and F are the wavelength corresponding to the highest band frequency in free space, the quality factor of metamaterial elements, the wave impedance in free space, the waveguide index and the coupling factor [34, 35]. In each mask, half of the elements are randomly turned on. In the simulations, two types of 3-D targets, point and distributed targets are considered, which are shown in Figures 2(a) and 2(b), respectively. In Figure 2(a), it is assumed that nine point scatterers (we call it Target 1) are located at $(-0.1,-0.1,0.46)$, $(-0.1,0.1,0.46)$, $(0.1,-0.1,0.46)$, $(0.1,0.1,0.46)$, $(0,0,0.5)$, $(-0.1,0,0.54)$, $(0,-0.1,0.54)$, $(0.1,0,0.54)$ and $(0,0.1,0.54)$, all in meters. The T-shaped target (we call it Target 2) in Figure 2(b) has dimensions of $0.2\times0.2\times0.01\text{m}^3$. According to the aperture size ($0.71\times0.71\text{m}^2$) and operating frequency, the targets are in the NF region [36, 37]. The number of voxels to define the scene is $105\times105\times111$. Isovalue in all isosurface is -10 dB. Figure 3 shows the pattern of k_z in terms of k_x and k_y according to the dispersion relation before making it uniform. It can be seen that unlike k_x and k_y which have a uniform distribution, k_z and the corresponding data in this form are not amenable to applying the fast IFT. That is why in Section 3, the use of Stolt interpolation before applying the IFT was described as one of the solutions to deal with it.

Table 1. The values of the main simulation parameters.

Parameter	f	N_f	N_T	N_R	d_T	d_R	M	Q	Z_0	n_g	F	z_0
Value	17.5-22 GHz	51	105	105	6.81 mm ($\lambda/2$)	6.81 mm ($\lambda/2$)	105	50	120π	2.5	1	1.1 m

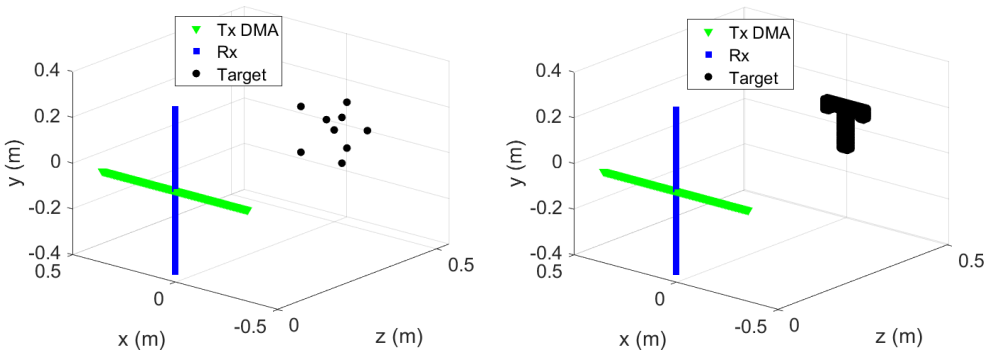

(a) (b)

Figure 2. A representation of two types of 3-D targets used in simulations; (a) nine point scatterers (Target 1), (b) T-shaped distributed target (Target 2).

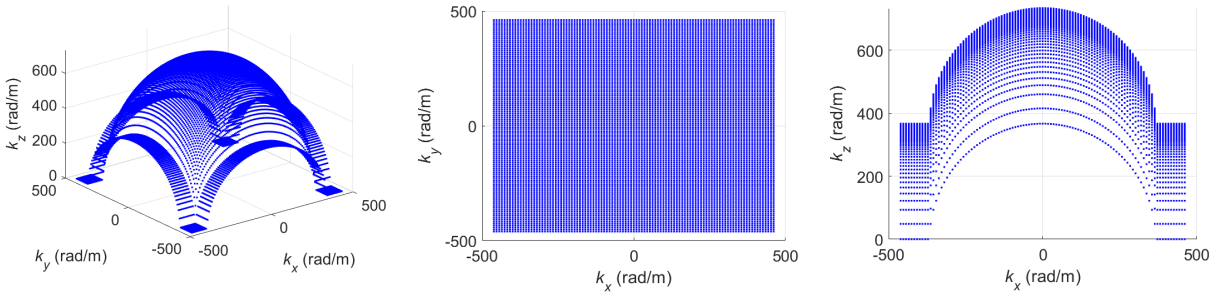

(a)

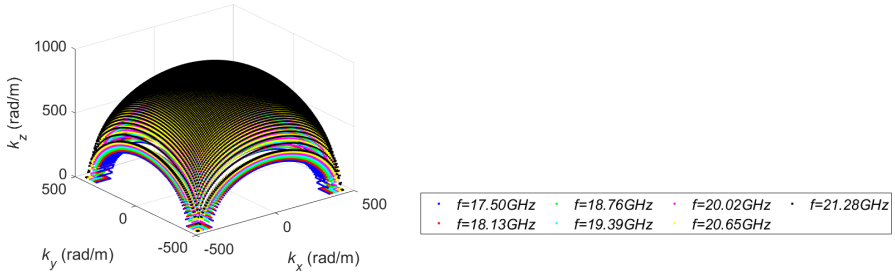

(b)

Figure 3. The pattern of k_x, k_y and k_z distributions; (a) at the frequency of 17.5 GHz, (b) at several various frequencies. The general pattern is independent of frequency; the only difference is the amplitude of k_z, which increases as expected with increasing frequency.

Figure 4 shows the reconstructed images of Target 1 using (7) and (8) assuming complete sampling. As can be seen, both approaches (i.e., using Stolt interpolation or using range stacking) work well. However, the computing times for the non-common steps of implementing these two algorithms are 0.41 and 1.09 seconds, respectively, which indicates that the first approach is faster. However, the advantage of the second approach is that due to multiple independent calculations on the range grid, it has the necessary potential for parallelization purposes. The distributed target outputs are shown in Figure 5. Both algorithms still work well. It is clear that the processing times are independent of the target type and are equal to the same values as before.

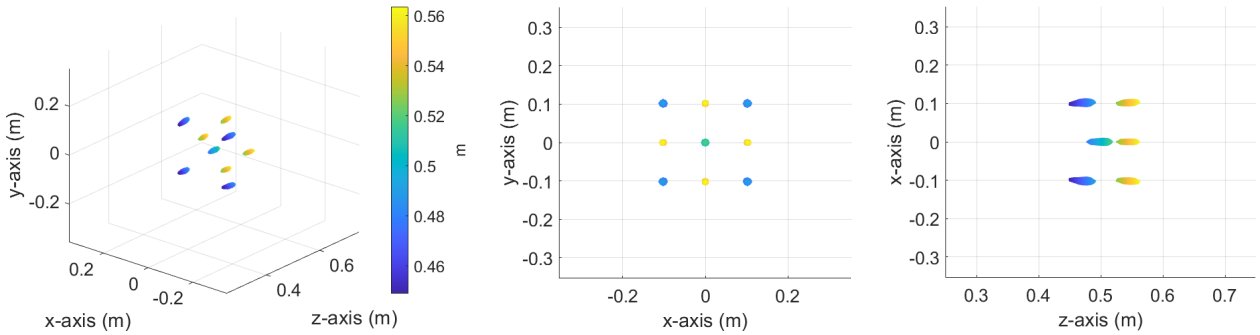

(a)

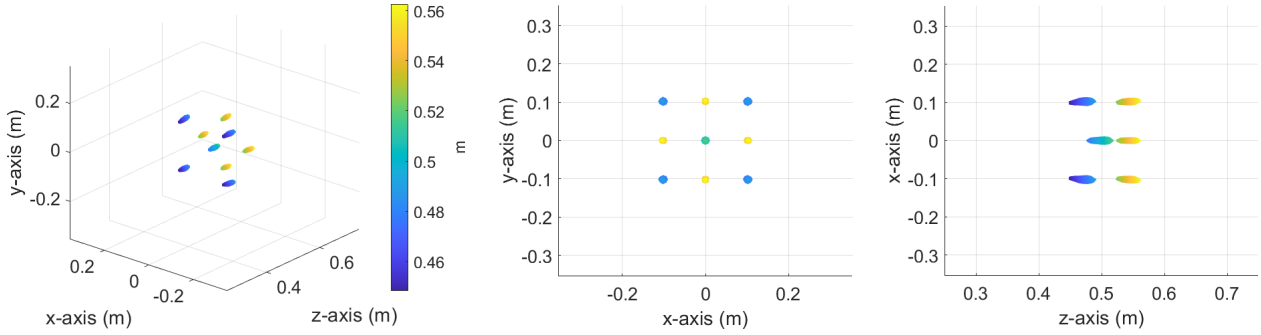

(b)

Figure 4. Reconstructed images of Target 1 in 2-D and 3-D views assuming full sampling; (a) by using (7), (b) by using (8).

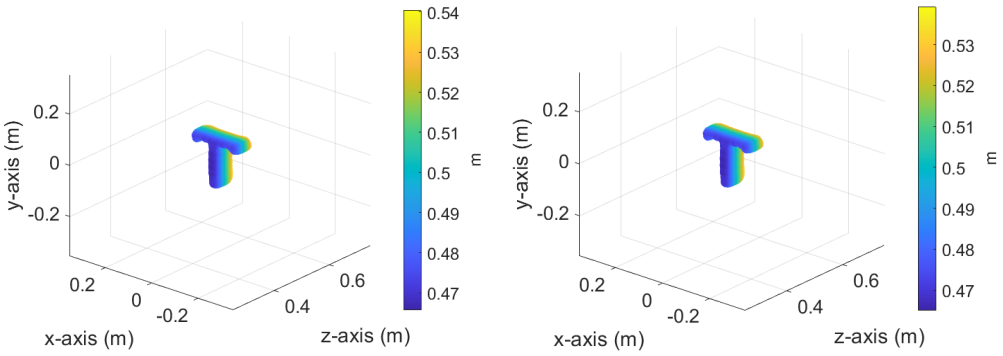

(a) (b)

Figure 5. Reconstructed images of Target 2 in 3-D view assuming full sampling; (a) by using (7), (b) by using (8).

In the following, we considered two sparse (and not full) sampling cases. In Case 1, it is assumed that only 50% of the frequency samples and 50% of the vertical scan samples are randomly considered. In Case 2, it is assumed that only 25% of the frequency samples are considered randomly (spatial sampling is full). Figure 6 shows an instance of the signals retrieved by the SL0 algorithm for Targets 1 and 2. The figures in the left column show the retrieved frequency signals at the point $(x_T = 0, y_R = 0)$. The figures in the right column show the recovered spatial signal in the vertical direction at the center frequency (19.75 GHz). Also, the root mean square error (RMSE) values corresponding to the diagrams in Figure 6 are given in Table 2. Note that these values are calculated in terms of normalized amplitudes (as the amplitudes are in Figure 6). In addition, the total RMSE (not for one sample as in Figure 6, but considering all recovered samples), that is, for data with dimensions of $105\times105\times51$, are given in Table 3. The values in Table 3 indicate that although in terms of CS rate [38], both Cases 1 and 2 have almost the same rate (about 26% for Case 1 and about 25% for Case 2), in

general, Case 1 suffers more errors. One reason for this may be that the DFT domain is a more suitable dictionary for frequency information.

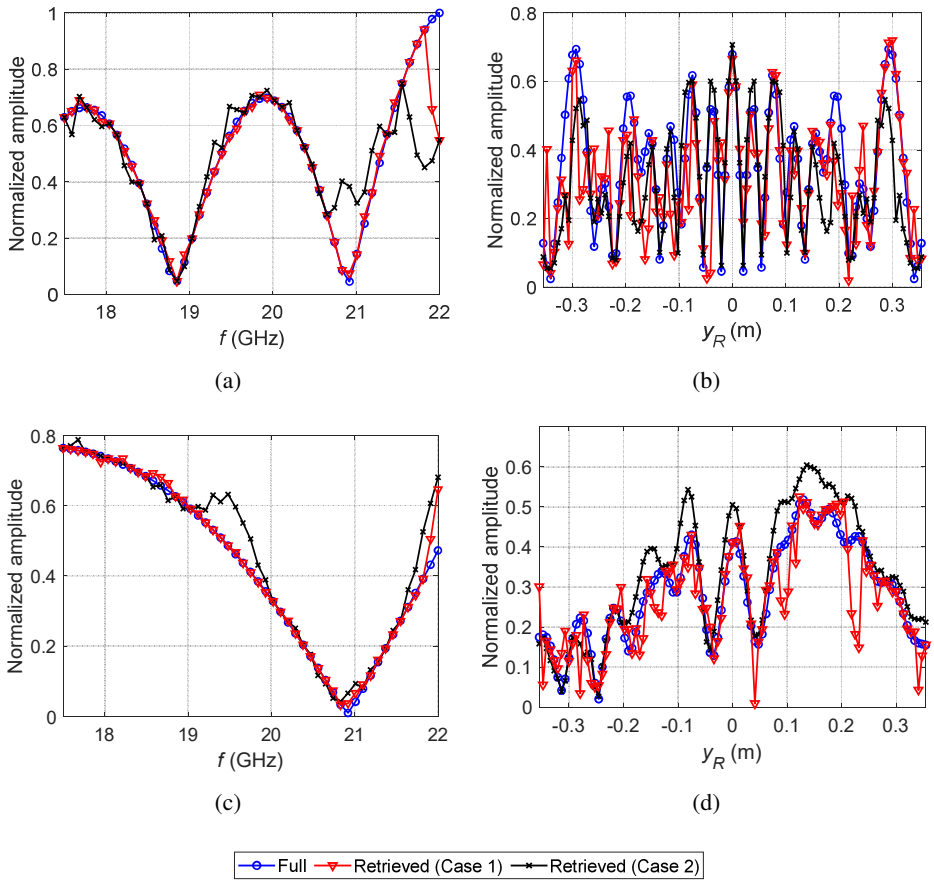

Figure 6. An instance of retrieved signals in the sparse sampling scenario; (a) frequency signals recovered at point $(x_T = 0, y_R = 0)$ for Target 1, (b) recovered vertical spatial signal at 19.75 GHz for Target 1, (c) frequency signals recovered at point $(x_T = 0, y_R = 0)$ for Target 2, (d) recovered vertical spatial signal at 19.75 GHz for Target 2.

Table 2. RMSE values corresponding to the diagrams in Figure 6.

Figure/Case	6(a)/1	6(a)/2	6(b)/1	6(b)/2	6(c)/1	6(c)/2	6(d)/1	6(d)/2
RMSE	0.0171	0.0646	0.0446	0.0300	0.0030	0.0117	0.0399	0.0077

Table 3. Total RMSE values.

Target/Case	1/1	1/2	2/1	2/2
RMSE	0.0376	0.0161	0.0139	0.0028

Finally, in Figure 7, the reconstructed images of Targets 1 and 2 in the sparse sampling scenario (both Cases 1 and 2) are shown using (7) and (8). Also, to provide a quantitative comparison, in Table 4, the normalized MSE (NMSE) [39] of these 8 reconstructed images are calculated, considering the corresponding Figures 4 and 5 as reference images. The results both visually and quantitatively show fewer errors in Case 2, which are consistent with the analyzes in the previous paragraph.

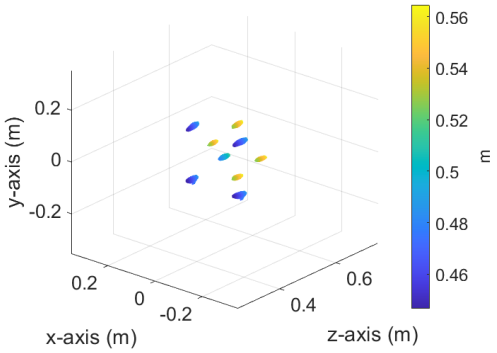
y-axis (m)
0.2
0
-0.2
x-axis (m)
0.2
0
-0.2
z-axis (m)
0.4
0.6
m
0.56
0.54
0.52
0.5
0.48
0.46

(a)

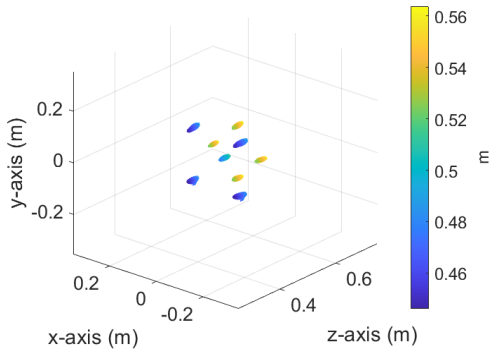
y-axis (m)
0.2
0
-0.2
x-axis (m)
0.2
0
-0.2
z-axis (m)
0.4
0.6
m
0.56
0.54
0.52
0.5
0.48
0.46

(b)

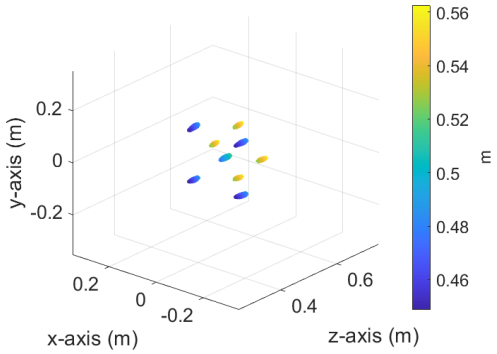
y-axis (m)
0.2
0
-0.2
x-axis (m)
0.2
0
-0.2
z-axis (m)
0.4
0.6
m
0.56
0.54
0.52
0.5
0.48
0.46

(c)

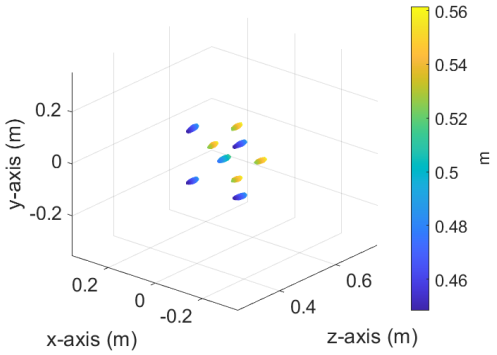
y-axis (m)
0.2
0
-0.2
x-axis (m)
0.2
0
-0.2
z-axis (m)
0.4
0.6
m
0.56
0.54
0.52
0.5
0.48
0.46

(d)

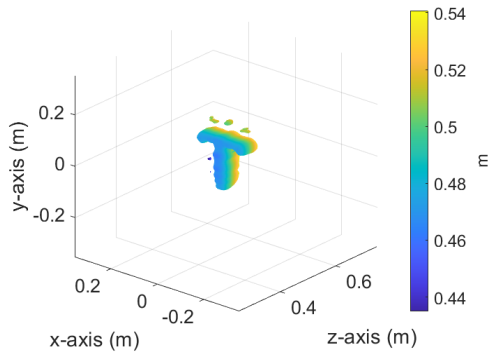
y-axis (m)
0.2
0
-0.2
x-axis (m)
0.2
0
-0.2
z-axis (m)
0.4
0.6
m
0.54
0.52
0.5
0.48
0.46
0.44

(e)

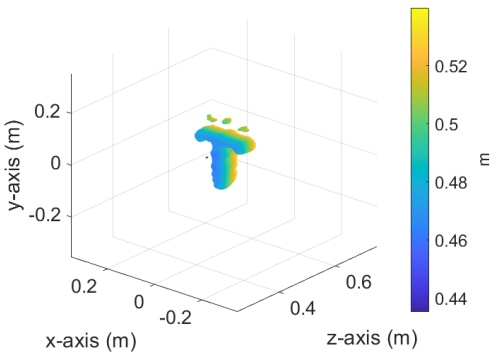
y-axis (m)
0.2
0
-0.2
x-axis (m)
0.2
0
-0.2
z-axis (m)
0.4
0.6
m
0.52
0.5
0.48
0.46
0.44

(f)

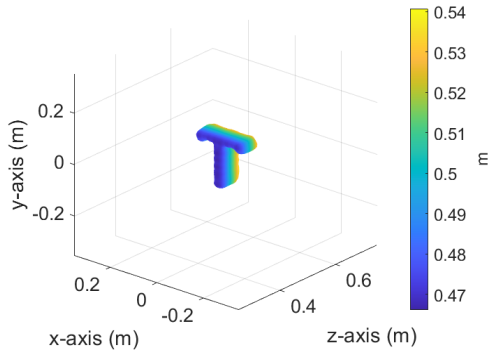
y-axis (m)
0.2
0
-0.2
x-axis (m)
0.2
0
-0.2
z-axis (m)
0.4
0.6
m
0.54
0.53
0.52
0.51
0.5
0.49
0.48
0.47

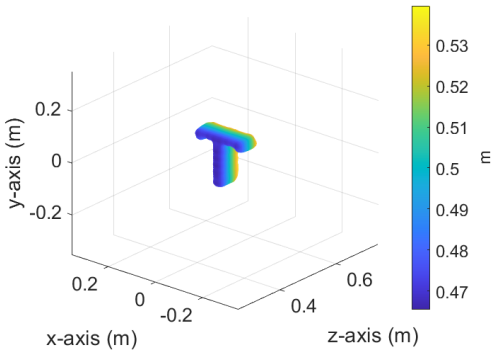
y-axis (m)
0.2
0
-0.2
x-axis (m)
0.2
0
-0.2
z-axis (m)
0.4
0.6
m
0.53
0.52
0.51
0.5
0.49
0.48
0.47

(g) (h)

Figure 7. Reconstructed images in sparse sampling scenario; (a) Target 1, Case 1, using (7), (b) Target 1, Case 1, using (8), (c) Target 1, Case 2, using (7), (d) Target 1, Case 2, using (8), (e) Target 2, Case 1, using (7), (f) Target 2, Case 1, using (8), (g) Target 2, Case 2, using (7), (h) Target 2, Case 2, using (8).

Table 4. NMSE of the reconstructed images in Figure 7.

Figure	7(a)	7(b)	7(c)	7(d)	7(e)	7(f)	7(g)	7(h)
NMSE	0.477	0.474	0.198	0.200	0.299	0.300	0.056	0.058

5. CONCLUSION

In this paper, a sparse frequency-spatial sampling scenario was considered for NF microwave imaging using DMA. Two methods of image reconstruction with and without the Stolt interpolation operator were studied for this scenario. The results of computer simulations confirmed the satisfactory performance of the designed approach. It was also shown that the DFT domain may not be a suitable dictionary for retrieving spatial samples as much as it is for retrieving frequency samples. To further improve the results in this particular case, more studies will be conducted in future work.

ACKNOWLEDGMENT

This work was funded by the Leverhulme Trust under Research Leadership Award RL-2019-019.

REFERENCES

[1] W. Shao and Y. Du, "Microwave imaging by deep learning network: Feasibility and training method," *IEEE transactions on antennas and propagation,* vol. 68, no. 7, pp. 5626-5635, 2020.

[2] N. Alam, A. Ahmed, M. A. I. Oni, T. A. Meem, and M. A. Rahman, "UWB microwave imaging for non-invasive anomaly detection in human lung and possible application in COVID-19 diagnosis: A review," in *2021 2nd International Conference on Robotics, Electrical and Signal Processing Techniques (ICREST)*, 2021: IEEE, pp. 772-776.

[3] A. M. Molaei, V. Skouroliakou, V. Fusco, and O. Yurduseven, "Efficient 3D image reconstruction for near-field microwave imaging using dynamic metasurface antenna," *IEEE Access,* vol. 10, pp. 68491-68498, 2022.

[4] O. Yurduseven, D. L. Marks, T. Fromenteze, J. N. Gollub, and D. R. Smith, "Millimeter-wave spotlight imager using dynamic holographic metasurface antennas," *Optics Express,* vol. 25, no. 15, pp. 18230-18249, 2017.

[5] O. Yurduseven, M. A. B. Abbasi, T. Fromenteze, and V. Fusco, "Frequency-diverse computational direction of arrival estimation technique," *Sci Rep,* vol. 9, no. 1, p. 16704, 2019.

[6] M. F. Imani *et al.*, "Review of metasurface antennas for computational microwave imaging," *IEEE transactions on antennas and propagation,* vol. 68, no. 3, pp. 1860-1875, 2020.

[7] T. Sleasman, M. F. Imani, A. V. Diebold, M. Boyarsky, K. P. Trofatter, and D. R. Smith, "Computational Imaging With Dynamic Metasurfaces: A Recipe for Simple and Low-Cost Microwave Imaging," *IEEE Antennas and Propagation Magazine,* vol. 64, no. 4, pp. 123-134, 2022.

[8] V. Skouroliakou, A. M. Molaei, M. García-Fernández, G. Álvarez-Narciandi, and O. Yurduseven, "Frequency Domain Image Reconstruction for Imaging With Multistatic Dynamic Metasurface Antennas," *IEEE Access,* vol. 10, pp. 124728-124737, 2022.

[9] A. M. Molaei, O. Yurduseven, and V. Fusco, "An efficient waveform diversity based on variational mode decomposition of coded beat-frequency shifted signals algorithm for multiple-input multiple-output millimetre-wave imaging," *IET Radar, Sonar & Navigation,* vol. 15, no. 10, pp. 1266-1280, 2021.

[10] A. M. Molaei, S. Hu, V. Skouroliakou, V. Fusco, X. Chen, and O. Yurduseven, "Fourier compatible near-field multiple-input multiple-output terahertz imaging with sparse non-uniform apertures," *IEEE Access,* vol. 9, pp. 157278-157294, 2021.

[11] A. M. Molaei, S. Hu, V. Skouroliakou, V. Fusco, X. Chen, and O. Yurduseven, "Fast processing approach for near-field terahertz imaging with linear sparse periodic array," *IEEE Sensors Journal,* vol. 22, no. 5, pp. 4410-4424, 2022.
[12] A. M. Molaei, S. Hu, V. Fusco, and O. Yurduseven, "A multi-resolution analysis-based approach to accelerate data acquisition for near-field MIMO millimeter-wave imaging," in *Passive and Active Millimeter-Wave Imaging XXV*, 2022, vol. 12111: SPIE, pp. 90-101.
[13] I. Yoo, "Analytic Model, Design of Waveguide-fed Metasurface Antennas and Applications to MIMO Communication Systems," Duke University, 2020.
[14] G. Lan *et al.*, "MetaSense: Boosting RF sensing accuracy using dynamic metasurface antenna," *IEEE Internet of Things Journal,* vol. 8, no. 18, pp. 14110-14126, 2021.
[15] V. Skouroliakou, A. M. Molaei, and O. Yurduseven, "Towards Real-Time Three-Dimensional (3D) Imaging using Dynamic Metasurface Antennas," in *European Conference on Antennas and Propagation*, 2023: IEEE.
[16] T. A. Sleasman, M. F. Imani, A. V. Diebold, M. Boyarsky, K. P. Trofatter, and D. R. Smith, "Implementation and characterization of a two-dimensional printed circuit dynamic metasurface aperture for computational microwave imaging," *IEEE Transactions on Antennas and Propagation,* vol. 69, no. 4, pp. 2151-2164, 2020.
[17] M. Boyarsky, T. Sleasman, M. F. Imani, J. N. Gollub, and D. R. Smith, "Electronically steered metasurface antenna," *Sci Rep,* vol. 11, no. 1, p. 4693, 2021.
[18] A. M. Molaei *et al.*, "Development of fast Fourier-compatible image reconstruction for 3D near-field bistatic microwave imaging with dynamic metasurface antennas," *IEEE Transactions on Vehicular Technology,* vol. 71, no. 12, pp. 13077-13090, 2022.
[19] A. M. Molaei, T. Fromenteze, S. Hu, V. Fusco, and O. Yurduseven, "Fourier-Based Near-Field Three-Dimensional Image Reconstruction in a Multistatic Imaging Structure Using Dynamic Metasurface Antennas," *IEEE Transactions on Computational Imaging,* vol. 8, pp. 1089-1100, 2022.
[20] A. V. Diebold, L. Pulido-Mancera, T. Sleasman, M. Boyarsky, M. F. Imani, and D. R. Smith, "Near-field SAR imaging with dynamic metasurface antennas using an adapted range migration algorithm," in *Computational Imaging III*, 2018, vol. 10669: SPIE, pp. 108-115.
[21] S. Han, D. Zhu, and X. Mao, "A modified space-variant phase filtering algorithm of PFA for bistatic SAR," *IEEE Geoscience and Remote Sensing Letters,* vol. 19, pp. 1-5, 2021.
[22] H. Gao *et al.*, "Study of the extended phase shift migration for three-dimensional MIMO-SAR imaging in terahertz band," *IEEE Access,* vol. 8, pp. 24773-24783, 2020.
[23] S. Jiacheng and M. Chen, "Research on imaging algorithm of millimeter wave radar based on stolt interpolation," in *2019 IEEE MTT-S International Microwave Biomedical Conference (IMBioC)*, 2019, vol. 1: IEEE, pp. 1-4.
[24] W. Wang, D. Wu, C. Hu, and H. Yu, "NUIFFT-RFT: A Novel Coherent Accumulation Method for Frequency agile Radar," in *2022 2nd International Conference on Computer Science, Electronic Information Engineering and Intelligent Control Technology (CEI)*, 2022: IEEE, pp. 287-293.
[25] R. He, B. Ai, G. Wang, M. Yang, C. Huang, and Z. Zhong, "Wireless channel sparsity: Measurement, analysis, and exploitation in estimation," *IEEE Wireless Communications,* vol. 28, no. 4, pp. 113-119, 2021.
[26] S. Thiruppathirajan, S. Sreelal, and B. Manoj, "Sparsity order estimation for compressed sensing system using sparse binary sensing matrix," *IEEE Access,* vol. 10, pp. 33370-33392, 2022.
[27] R. Obermeier and J. A. Martinez-Lorenzo, "Sensing matrix design via mutual coherence minimization for electromagnetic compressive imaging applications," *IEEE Transactions on Computational Imaging,* vol. 3, no. 2, pp. 217-229, 2017.
[28] Z. Zhou, "RIP analysis for the weighted ℓr-ℓ1 minimization method," *Signal Processing,* vol. 202, p. 108754, 2023.
[29] A. M. Molaei, R. Kumar, S. Hu, V. Skouroliakou, V. Fusco, and O. Yurduseven, "A compressive sensing-based approach for millimeter-wave imaging compatible with Fourier-based image reconstruction techniques," in *2022 23rd International Radar Symposium (IRS)*, 2022: IEEE, pp. 87-91.
[30] A. Aghasi, A. Ahmed, P. Hand, and B. Joshi, "Bilinear compressed sensing under known signs via convex programming," *IEEE Transactions on Signal Processing,* vol. 68, pp. 6366-6379, 2020.
[31] Q. Deng *et al.*, "Compressed sensing for image reconstruction via back-off and rectification of greedy algorithm," *Signal Processing,* vol. 157, pp. 280-287, 2019.
[32] H. Ren, H. Pan, S. I. Olsen, and T. B. Moeslund, "Greedy vs. l1 convex optimization in sparse coding: Comparative study in abnormal event detection," in *ICML'15 Workshop: FEAST 2015: ICML Workshop on Features and Structures*, 2015.

[33] T. E. Komolafe *et al.*, "Smoothed L0-constraint dictionary learning for low-dose X-ray CT reconstruction," *IEEE Access,* vol. 8, pp. 116961-116973, 2020.
[34] D. R. Smith, O. Yurduseven, L. P. Mancera, P. Bowen, and N. B. Kundtz, "Analysis of a waveguide-fed metasurface antenna," *Physical Review Applied,* vol. 8, no. 5, p. 054048, 2017.
[35] M. F. Imani, T. Sleasman, and D. R. Smith, "Two-dimensional dynamic metasurface apertures for computational microwave imaging," *IEEE Antennas and Wireless Propagation Letters,* vol. 17, no. 12, pp. 2299-2303, 2018.
[36] A. M. Molaei, P. del Hougne, V. Fusco, and O. Yurduseven, "Efficient joint estimation of DOA, range and reflectivity in near-field by using mixed-order statistics and a symmetric MIMO array," *IEEE Transactions on Vehicular Technology,* vol. 71, no. 3, pp. 2824-2842, 2021.
[37] A. M. Molaei, P. Del Hougne, V. Fusco, and O. Yurduseven, "Numerical-Analytical Study of Performance of Mixed-Order Statistics Algorithm for Joint Estimation of DOA, Range and Backscatter Coefficient in a MIMO Structure," in *2022 23rd International Radar Symposium (IRS)*, 2022: IEEE, pp. 396-401.
[38] M. Rani, S. B. Dhok, and R. B. Deshmukh, "A systematic review of compressive sensing: Concepts, implementations and applications," *IEEE access,* vol. 6, pp. 4875-4894, 2018.
[39] A. M. Molaei, S. Hu, R. Kumar, and O. Yurduseven, "MIMO Coded Generalized Reduced Dimension Fourier Algorithm for 3D Microwave Imaging," *IEEE Transactions on Geoscience and Remote Sensing,* vol. 61, 2023.